Simultaneous ambient pressure x-ray photoelectron spectroscopy and grazing incidence x-ray scattering in gas environments

Heath Kersell, [iD] Pengyuan Chen, Henrique Martins, Qiyang Lu, [iD] Felix Brausse, Bo-Hong Liu, Monika Blum, Sujoy Roy, Bruce Rude, [iD] Arthur Kilcoyne, [iD] Hendrik Bluhm, and [iD] Slavomír Nemšák

View Online   **Export Citation**   **CrossMark**

ARTICLES YOU MAY BE INTERESTED IN

Ultrafast extreme ultraviolet photoemission electron microscope
Review of Scientific Instruments **92**, 043709 (2021); https://doi.org/10.1063/5.0047076

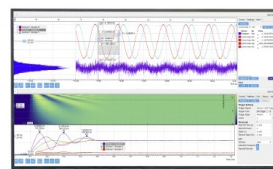Ambient pressure mapping of resonant Auger spectroscopy at BL02B01 at the Shanghai Synchrotron Radiation Facility
Review of Scientific Instruments **91**, 123108 (2020); https://doi.org/10.1063/5.0020469

Billion-pixel x-ray camera (BiPC-X)
Review of Scientific Instruments **92**, 043708 (2021); https://doi.org/10.1063/5.0043013

Simultaneous ambient pressure x-ray photoelectron spectroscopy and grazing incidence x-ray scattering in gas environments

View Online   Export Citation   CrossMark

Heath Kersell,[1] Pengyuan Chen,[2] (ID) Henrique Martins,[1,3] Qiyang Lu,[1,4] Felix Brausse,[5] (ID) Bo-Hong Liu,[1,5] Monika Blum,[1,5] Sujoy Roy,[1] Bruce Rude,[1] Arthur Kilcoyne,[1] (ID) Hendrik Bluhm,[1,5,6] and Slavomír Nemšák[1,a)] (ID)

AFFILIATIONS

[1] Advanced Light Source, Lawrence Berkeley National Laboratory, Berkeley, California 94720, USA
[2] Department of Electrical Engineering and Computer Sciences, University of California, Berkeley, California 94720, USA
[3] Department of Physics, University of California, Davis, California 95616, USA
[4] Department of Materials Science and Engineering, Stanford University, Stanford, California 94305, USA
[5] Chemical Science Division, Lawrence Berkeley National Laboratory, Berkeley, California 94720, USA
[6] Department of Inorganic Chemistry, Fritz Haber Institute of the Max Planck Society, 14195 Berlin, Germany

[a)]Author to whom correspondence should be addressed: SNemsak@lbl.gov

ABSTRACT

We have developed an experimental system to *simultaneously* measure surface structure, morphology, composition, chemical state, and chemical activity for samples in gas phase environments. This is accomplished by simultaneously measuring x-ray photoelectron spectroscopy (XPS) and grazing incidence x-ray scattering in gas pressures as high as the multi-Torr regime while also recording mass spectrometry. Scattering patterns reflect near-surface sample structures from the nano-scale to the meso-scale, and the grazing incidence geometry provides tunable depth sensitivity of structural measurements. Scattered x rays are detected across a broad range of angles using a newly designed pivoting-UHV-manipulator for detector positioning. At the same time, XPS and mass spectrometry can be measured, all from the same sample spot and under ambient conditions. To demonstrate the capabilities of this system, we measured the chemical state, composition, and structure of Ag-behenate on a Si(001) wafer in vacuum and in O_2 atmosphere at various temperatures. These simultaneous structural, chemical, and gas phase product probes enable detailed insights into the interplay between the structure and chemical state for samples in gas phase environments. The compact size of our pivoting-UHV-manipulator makes it possible to retrofit this technique into existing spectroscopic instruments installed at synchrotron beamlines. Because many synchrotron facilities are planning or undergoing upgrades to diffraction limited storage rings with transversely coherent beams, a newly emerging set of coherent x-ray scattering experiments can greatly benefit from the concepts we present here.

I. INTRODUCTION

Nano- and atomic-scale understanding of chemical and structural processes is highly sought-after in many technologically relevant areas: from photovoltaics[1] and information storage[2] to batteries[3] and heterogeneous catalysis.[4] Additionally, practically all important technological or natural processes take place in ambient gas environments. These environments often induce complex relationships between structure, chemistry, and function. For example, as dimensions reach the nanoscale, transition metals and transition metal oxides exhibit size dependent behavior, contributing to heavy metal migration in geological systems.[5–7] Reactant gas environments can lead to pressure-dependent adsorbate coverages[8–10] and potentially initiate nanocluster formation at catalyst surfaces, subsequently altering reaction pathways.[8,11,12] Active species in bimetallic alloy catalysts can segregate under reaction conditions, altering their operando surface composition.[13,14] Polyamide membranes for water purification exhibit correlations between water permeability and the

presence of nanoscale Turing structures.[15] A detailed understanding of the correlation between chemistry, structure, and function in these systems requires multimodal investigations. Additionally, each of these processes occurs in heterogeneous environments, and measuring them in ambient gas mixtures requires *in situ* or operando techniques.

In the past two decades, a number of operando spectroscopic and structural probes were developed to study heterogeneous interfaces.[16,17] For example, environmental transmission electron microscopy (ETEM) enables cross-sectional elemental mapping in ambient pressure environments.[18] Polarization-modulation infrared reflection-absorption spectroscopy (PM-IRRAS) provides an operando probe of interfacial adsorbates.[16] Dynamic surface restructuring at pressures from ultrahigh vacuum (UHV) to the bar regime can be measured with atomic resolution using high pressure scanning tunneling microscopy (HPSTM) and atomic force microscopy (HPAFM).[17,19,20] Operando studies of surface chemical composition and chemical states, as well as adsorbate species, can be pursued with ambient pressure x-ray photoelectron spectroscopy (APXPS).[21]

In spite of the growth of operando methods over the last two decades, understanding the detailed relationship between dynamic surface restructuring and chemical transformations remains a difficult task. One challenge lies in correlating chemical transformations with structural evolutions, each measured with separate techniques. This is often done using separate samples, separate measurement sets, and frequently in entirely separate experimental systems. Across experimental systems, differences in pressure measurements, sample temperatures, time resolutions, and sample quality can lead to difficulties comparing structural and chemical changes in separate measurements. This opens a gap between the two experiments, complicating the interpretation of separately collected data and hindering the accuracy of such separate experiments. Therefore, multimodal approaches, such as the one presented in this work, have been undertaken at various synchrotron facilities with a few successful results. For example, a combined APXPS and IRRAS study utilized the sensitivity introduced by IRRAS to identify species that were not detected in APXPS measurements.[22] Some experimental systems are now also equipped to measure x-ray based spectroscopies and x-ray diffraction (XRD).[23] For example, a setup at the Argonne National Laboratory allows for simultaneous analysis of chemistry and structure using hard x-ray photoelectron spectroscopy and XRD in a specifically designed pulsed laser deposition chamber.[24] To address the need for simultaneous structural and chemical probes under ambient conditions, we have combined APXPS with grazing incidence x-ray scattering (GIXS). This combination enables the *simultaneous* correlation of sample chemical states and adsorbate species, with surface structures that emerge in heterogeneous environments, where ambient pressures reach into the Torr regime.

II. COMBINING AMBIENT PRESSURE PHOTOEMISSION AND X-RAY SCATTERING

In XPS, x-ray photons incident on a material cause photoelectron emission if the photon energy exceeds the binding energy of electrons in the material. The resulting photoelectron intensity at various kinetic energies provides information about surface chemistry, composition, valence states, and adsorbate coverage.[25] Because

electrons are strongly scattered by matter, these photoelectrons are predominantly from the surface and near-surface regions, with typical probing depths in the few nm range. Electrons are also strongly scattered by gas molecules, and thus, most XPS experiments are performed in high or ultrahigh vacuum conditions. To measure under ambient pressures, APXPS apparatuses are equipped with a small (sub-mm) aperture in front of the sample surface, which photoelectrons pass through.[21,26] This aperture leads to a differentially pumped electrostatic lens system and then to a hemispherical electron energy analyzer, as shown in Fig. 1.[27] The differential pumping strongly reduces scattering of photoelectrons in the lens system by gas molecules, allowing them to reach the hemispherical analyzer where differential pumping maintains high vacuum.

While some photons incident on the sample are absorbed to produce photoelectrons, some are also elastically scattered. The resulting scattering pattern reflects the arrangement of scattering centers in the sample (i.e., the sample structure). X rays incident at grazing angles enable x-ray scattering measurements in the reflection geometry (as in Fig. 1),[28] opposite to the transmission geometry, allowing simultaneous measurements of ambient pressure GIXS (APGIXS) and APXPS.

X rays scattered from samples form an interference pattern with maxima (constructive interference) at angles inversely related to the location of the scattering centers. When the scattering patterns are generated by x rays at grazing incidence, the corresponding x-ray scattering techniques are broadly grouped into grazing incidence wide angle x-ray scattering (GIWAXS) and grazing incidence small angle x-ray scattering (GISAXS).

Depending on the wavelength of the incident x rays, GIWAXS provides access to atomic scale information at large scattering angles, making it ideal for studies of crystal structures and their transformations.[29,30] Meanwhile, at smaller scattering angles, GISAXS has been applied to the study of more extended structures in thin film growth, nanoparticle stability, block copolymer thin film evolution, and quantum dots, for example Refs. 31–34. There is no unambiguous delineation between the small- and wide-angle regimes in GIXS, and combined GISAXS/GIWAXS investigations provide a detailed picture of crystal structures and the growth or evolution of structures from the nanoscale to the mesoscale.[35]

III. DESCRIPTION OF THE EXPERIMENTAL APPARATUS

Measurement of GIXS across the small- and wide-angle regimes in ambient gas environments poses a number of challenges. For example, simultaneous APGIXS and APXPS measurements require (i) that x rays be incident on samples at positions that optimize the photoelectron intensity reaching the analyzer, while also scattering into angles accessible by the x-ray detector. Detecting structures from the atomic-scale to the meso-scale also requires a detector capable of both (ii) measurement over a wide range of scattering angles and (iii) high angular resolution (especially for coherent scattering and observing speckles). Additionally, (iv) the photon detector itself often needs to be in vacuum, isolated from gas phase sample environments.

To address these issues, we developed the experimental configuration illustrated in Fig. 1. In this layout, a custom UHV sample
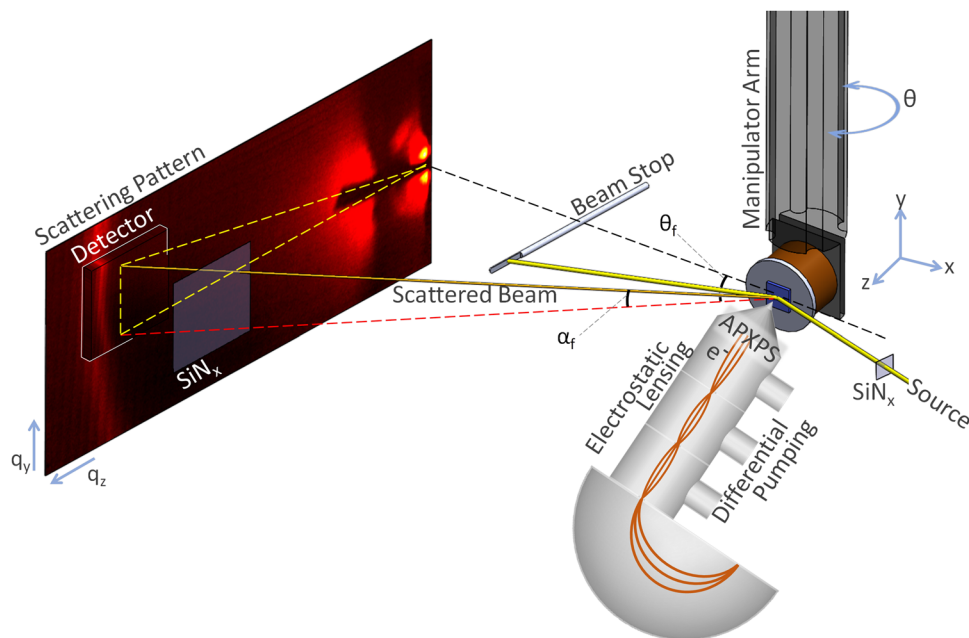
FIG. 1. Schematic of a combined ambient pressure XPS/GIXS system. X rays from the source (beamline, right side) enter the sample chamber through a silicon nitride (SiN$_x$) window (blue, right). Photoelectrons are collected by the differentially pumped electrostatic lens system and analyzer (bottom), which are separated from the sample environment by a small aperture near the sample surface. Photons scattered from the sample are measured by a detector (left side). A SiN$_x$ window separates the x-ray detector from the gas environment. X-ray scattering angles (θ_f, α_f) correspond to specific q$_y$ and q$_z$.

chamber is connected to the x-ray source at beamline 11.0.2 of the Advanced Light Source in Berkeley[36] with a practical photon energy range of 180–1800 eV. The chamber is also connected to a differentially pumped commercial APXPS analyzer (SPECS Phoibos 150 NAP), as well as a moveable differentially pumped x-ray detector (Andor iKon-L SO CCD). X-ray transparent silicon nitride windows separate the sample environment from both the x-ray source (beamline) and the x-ray detector. The APXPS detector is separated from the sample environment by differential pumping stages, as discussed in Sec. II. A four-axis sample manipulator enables linear sample translation in three dimensions and polar angle rotation. Although not shown in Fig. 1, the chamber is also connected to a sample preparation and load-lock chamber, providing basic surface science type treatments, such as Ar$^+$ bombardment. How this layout addresses the challenges (i)–(iv) enumerated in the previous paragraph is discussed next.

A. Addressing challenge (i)

A commercially available four-axis manipulator (Thermionics Inc.) enables three dimensional cartesian positioning of the sample, and polar rotation with respect to both the x-ray beam source and the APXPS analyzer. Control over the sample polar angle facilitates sample alignment such that grazing incidence x rays generate photoelectrons, which enter the APXPS aperture, while some photons simultaneously scatter from the sample toward the detector. In our system, a ~100 μm wide x-ray beam is incident on the sample surface ~0.5 mm from the 0.3 mm wide APXPS aperture. When the x-ray beam is at grazing incidence with respect to the sample surface, this

geometry elongates the x-ray beam along the beam direction, generating scattered x rays from an elongated sample region. This can cause a mismatch between the field of view of the APXPS analyzer and the area from which scattered x rays are collected. Several solutions exist for this problem. One is to focus down or clip the x-ray beam with an aperture, decreasing the area of the beam illuminating the sample to match the analyzer's field of view. Alternatively, sample areas equal to or smaller than the analyzer field of view limit the scattering area to the same region APXPS is collected from. This is especially applicable to engineered samples prepared by lithography, where the patterned area can be matched with the hemispherical analyzer field of view. Additionally, homogeneous samples can be used, rendering the measurements insensitive to the sample region where data are collected.

The grazing incidence geometry, facilitated by polar angle control, also enables control over the information depth for these techniques. The penetration depth of x rays drastically decreases with decreasing incidence around the critical angle, which can be as high as several degrees at 1000 eV. Meanwhile, the emission angle in XPS affects the depth contribution of photoelectrons reaching the analyzer. We note that, in principle, a transmission scattering geometry could also be used, although the sample thickness becomes an important consideration in that case.

B. Addressing challenge (ii)

To measure GIXS over a wide range of scattering angles, we developed a new pivoting-UHV-manipulator capable of scanning an x-ray detector in two angular dimensions [Fig. 2(a)]. As shown
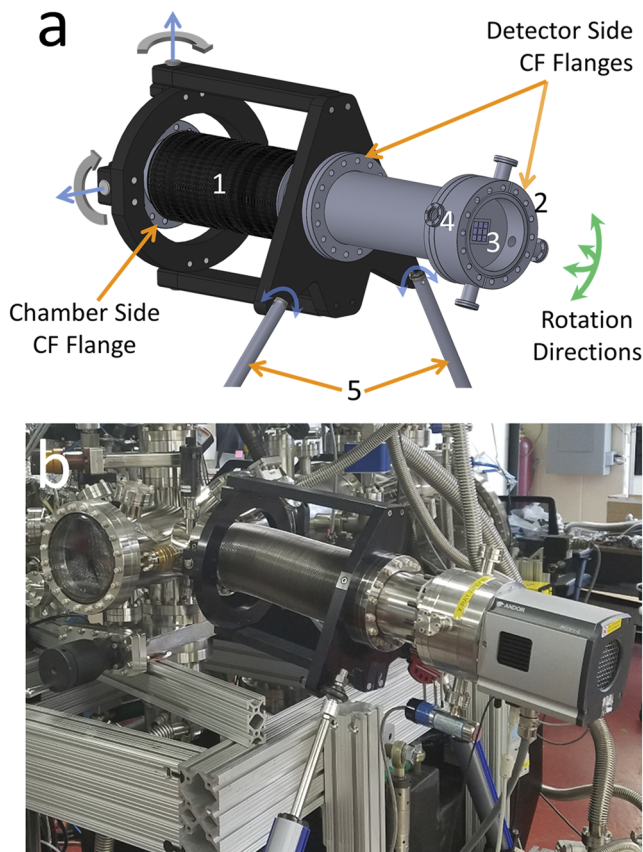
FIG. 2. Pivoting-UHV-manipulator. The model (a) and picture (b) show an edge welded bellows (1) attached to two CF flanges. The chamber side CF flange is rigidly attached to a UHV chamber. The whole assembly pivots around two bearings at the chamber side, allowing them to independently rotate about the bearing axes (blue arrows). This enables detector motion through a solid angle (green curved arrows) with ~±12° around either axis. The detector is mounted on the CF flange at the right (2), where a 150 nm thick silicon nitride window (3) separates it from gases in the sample chamber. The volume between the window and detector can be pumped through one of the CF mini ports (4). Detector motion is controlled by a pair of approximately orthogonal precision linear actuators (5).

in Fig. 2, this device is attached to our vacuum chamber by a 6 in. CF flange at one end [left side of Fig. 2(a)]. At the opposite end is a 6 in. CF flange where a vacuum compatible x-ray detector can be mounted [right side of Fig. 2(a)]. UHV is maintained between these two sides by a combination of flexible edge welded bellows, 4 in. stainless steel tubes, and 6 in. CF flanges. At the chamber-side, the pivoting-UHV-manipulator contains a pair of rotation axes that enable movement of the detector in two angular dimensions [straight blue arrows in Fig. 2(a)]. The vacuum bellows is flexible, bending and maintaining vacuum when the detector is moved. Detector motion is controlled by a pair of precision linear actuators, with a step resolution of 10 μm. The top of each actuator is attached to the pivoting-UHV-manipulator by a rotatable ball joint so that actuator extensions or retractions precisely translate the manipulator across two angular directions [Fig. 2(a)]. Each actuator base is

connected to a universal joint fixed to the system frame (not shown), allowing the actuators to pivot while controlling the detector position. This layout facilitates movement of the detector in two angular directions across a pseudo-spherical cap, illustrated by green curved arrows at the right side of Fig. 2(a). An important aspect of x-ray scattering measurements is the range of available scattering angles where the camera has direct, unobstructed line-of-sight to the sample. This range is primarily determined by the size and position of the main vacuum flange between the chamber and pivoting-UHV-manipulator. This set of unobstructed angles determines the range over which scattered x rays can be detected and is illustrated in Fig. 1 by the red arrow scattered by the sample. We optimized this range, and the range of detector motion, to coincide with x-ray scattering angles relevant to many ambient pressure investigations. Scattered x rays beyond the angular range represented by the red arrow in Fig. 1 will be obstructed. In our present layout, the angular range can be as large as ~±12° azimuthally and 0° to +24° in the polar direction (with respect to the sample), which accommodates measurement of features as small as ~2 nm for the photon energy range available at beamline 11.0.2 at the ALS. This range can be increased by using a larger diameter bellows and a larger port on the chamber, which provides more space for scattered x rays to pass unobstructed to the detector. This design facilitates GIXS measurements in both the small-angle and wide-angle regimes. One major advantage of this design is its relatively compact size. As shown in Fig. 2(b), the entire pivoting-UHV-manipulator, which moves the x-ray detector, is not much larger than our eight-inch-wide UHV sample chamber. This is significantly smaller than conventional SAXS flight tubes by approximately an order of magnitude or more. As a result, this design can be implemented for GIXS measurements in existing systems whose size is constrained by the amount of experiment floor available around the instrument.

C. Addressing challenge (iii)

One critical experiment that requires high angular resolution is coherent x-ray scattering. Coherent illumination of a distribution of scattering centers gives rise to a so-called "speckle pattern," which is characterized by interference of photons scattered by that distribution. Changes in the speckle pattern can be measured to understand changes in the distribution of scattering centers. To extract meaningful information about the evolution of scattering center distributions in such measurements, a detector must have resolution at least as fine as the speckle size, σ, which depends on the photon wavelength, λ, the distance between the sample and detector, D, and the width of the coherently illuminated area, a, as[37]

$$\sigma = \frac{\lambda D}{a}. \tag{1}$$

In the experimental setup described in this section, we use a CCD camera as our detector, with 2048×2048 pixels^2 and 13.5×13.5 μm^2 pixel size (Andor iKon-L SO). Given formula (1), the minimum sample–detector distance for a 30 μm spot-size and 1.5 keV radiation at beamline 11.0.2.1 of the Advanced Light Source is ~50 cm. To measure with high angular resolution across the small- and wide-angle regimes and facilitate future coherent scattering experiments, the pixel size of the detector and its positioning require a resolution on the order of ~10 μm. Such conditions are

necessary to pursue more sophisticated investigations of structural dynamics.

Matching the speckle size and the detector resolution is, however, not the only condition that needs to be met in order to perform coherent scattering experiments. With the current photon source, only a small central portion of the beam is coherent. Therefore, a small aperture ($<10 \times 10 \ \mu m^2$ SiN_x window) selecting this part of the beam would be installed at the beamline/chamber interface. The mechanical stability of the system (beam aperture at the chamber entrance, the sample, and detector positions) also has to be sufficient to maintain a consistent speckle pattern. Last but not least, the x-ray optics and x-ray transmissive windows, both between the photon source and sample and between the sample and detector, will influence the shape of the wave-front and impact the coherent properties of the light. We expect that wave-front distortion by x-ray windows will be a manageable problem, similarly to hard x-ray coherent scattering beamlines, which use thick beryllium windows. All these issues have to be addressed before such experiments, and further details will be a scope of future publications. Still, inclusion of these features in the system design is necessary to accommodate future coherent scattering measurements.

D. Addressing challenge (iv)

Using a CCD camera for measuring scattered x rays presents a unique challenge in ambient pressure environments. To lower electronic thermal noise, CCD detectors are usually cooled using multiple-stage Peltier elements. As a result, any humidity or other condensable gases can coat the camera surface, causing electrical shorts and artifacts in the imaging, and inevitably reducing the lifetime of the camera. It is therefore necessary to isolate the detector from the gas phase sample environments. For the experimental setup described in this section, this is accomplished using a 150 nm thick x-ray transparent silicon nitride membrane with an area of $27 \times 27 \ mm^2$ (Silson Ltd.). The window is divided into a 3×3 array of $8.33 \times 8.33 \ mm^2$ sections, divided by 1 mm thick frames, which enhance the membrane stability against high pressure differentials [Fig. 2(a)]. Scattered x rays pass through the silicon nitride membrane to reach the CCD detector, while the membrane isolates the CCD chip from the gas phase environment of the sample chamber. These membranes are stable up to pressure differentials of several tens of Torr, which enables x-ray scattering measurements in ambient pressure gas environments across a similar pressure regime to that accessible in our APXPS system (<20 Torr). This has the added benefit of protecting the CCD chip from corrosive gases, enabling the study of a number of additional systems in, e.g., corrosion science. A set of four 1.33 in. CF flanged ports on the camera side of the x-ray window (shown in Fig. 2) enables the use of differential pumping, pressure measurement, and other diagnostic devices (e.g., a photodiode and a beam stop). We also note that during the measurements shown in Sec. IV, a beam stop prevented the CCD camera from saturation by the reflected beam [Figs. 3(b)–3(d)]. It was mounted on a 1.33 in. CF flange on the chamber, with motion controlled by a pair of orthogonally positioned UHV linear feedthroughs. One feedthrough enables insertion or retraction of the beam stop into or from the beam path. The other can mechanically tilt the beam stop to adjust its position perpendicular to the scattering plane. To monitor the gas composition, including the formation of reaction products, we also installed a quadrupole mass spectrometer in the first differential pumping stage of the electrostatic lensing system (Fig. 1), where the pressure is about four orders of magnitude lower than in the sample chamber. This enables mass spectrometry measurements to accompany the aforementioned APXPS and APGIXS. Mass spectrometers are by now a standard part of practically all APXPS systems around the world, and they are used primarily in the field of catalysis. Finally, *in situ* sample preparation is enabled by a sample heater and thermocouple on the sample manipulator and by an ion gun and gas leak valves in the preparation chamber.

IV. PROOF-OF-PRINCIPLE MEASUREMENTS OF Ag-BEHENATE

To confirm the capabilities of this newly built system, we measured changes in Ag-behenate ($AgC_{22}H_{43}O_2$) layers deposited on SiO_x as a function of temperature in the presence of O_2 gas. The Ag-behenate molecule [Fig. 3(a)] contains a long-chain silver carboxylate, which, when deposited onto a substrate, forms dimers that arrange into a layer-by-layer structure with an interlayer spacing of ~5.84 nm. Because of its regular interlayer spacing, Ag-behenate is a
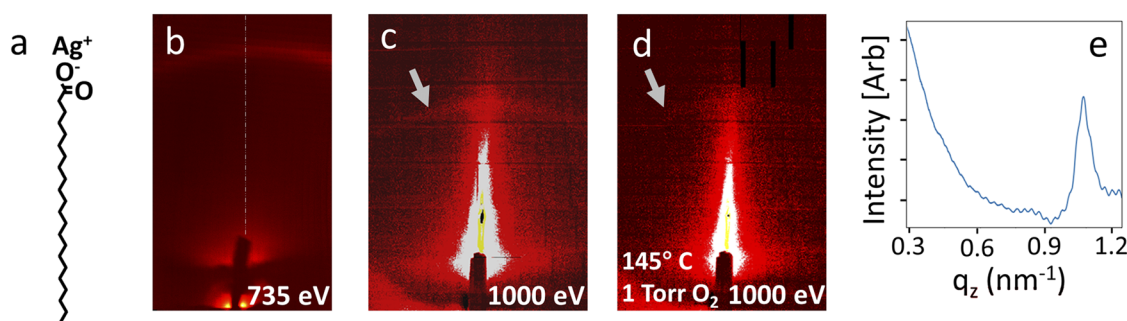

FIG. 3. X-ray scattering from Ag-behenate. (a) Ag-behenate molecular structure. (b) Scattering pattern containing the first order x-ray scattering peak from Ag-behenate. (c) Low exposure acquisition (117 s) of the Ag-behenate scattering pattern. A gray arrow designates the scattering intensity maximum from the Ag-behenate layers. (d) Low exposure acquisition of the Ag-behenate scattering pattern after heating in oxygen gas. The gray arrow designates the location where the scattering feature from Ag-behenate layers existed before heating. (e) Intensity line profile across the vertical centerline shown in the scattering pattern in (b). Note that 735 eV photons were used in (b), and 1000 eV photons were used to produce (c) and (d).

common reference standard in x-ray scattering experiments.[38,39] Its layered structure yields a scattering pattern characterized by rings of high intensity at $Q = 0.108$ Å^{-1} and at successively higher order scattering maxima.[40] In our measurements, Ag-behenate was deposited onto a Si(001) surface covered by a native oxide layer by drop-casting a Ag-behenate-in-ethanol solution onto the surface and allowing the solution to dry in air. Once placed in vacuum, this system generated a clear scattering pattern in our GIXS measurements, shown in Fig. 3(b). The intensity line profile across the vertical centerline [Fig. 3(e)] shows a clear peak at 0.108 Å^{-1}, as expected. We note that the intensity of the scattering feature decreases somewhat from the side of the image in Fig. 3(b) where the recording was started (right) to the end (left), suggesting that over the course of the image, some beam damage may occur. The x-ray sample exposure during this acquisition was ~5×10^{15} photons.

As a result, we recorded the images shown in Figs. 3(c) and 3(d) and the spectra shown in Fig. 4 on a fresh sample, with
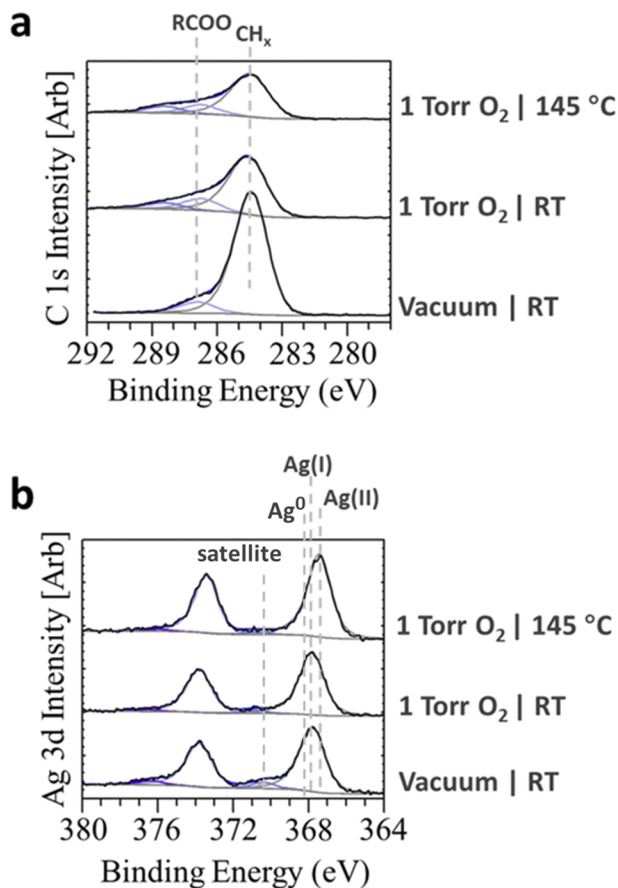

FIG. 4. (a) APXPS of the C 1s region on Ag-behenate under various conditions. Three features appear at 283.8 (C–C), 285.9 (RCOO), and 287 eV. The higher BE peak is characteristic of more highly oxidized carbon species in response to added oxygen. (b) Ag 3d region. Positions are shown for Ag$^+$ in Ag-behenate, metallic Ag^0, and Ag^{2+} upon heating in O$_2$(g). Each spectrum in (a) and (b) is fitted with a Shirley background shape, represented by a gray line at the base of each spectrum. Photons with 1000 eV excitation energy were used to collect the C 1s and Ag 3d spectra.

significantly smaller exposure to the x-ray beam to mitigate beam damage. The total exposure during x-ray scattering and APXPS measurements in the case of Figs. 3(c), 3(d), and 4 was ~3.5×10^{14} photons per condition, more than an order of magnitude lower than for the image in Fig. 3(b). Figure 3(c) shows the x-ray scattering pattern of an as-prepared Ag-behenate/Si(001) at a fresh spot. Due to the different incident photon energy used to collect Fig. 3(c) compared to Fig. 3(b) (1000 eV vs 735 eV), the scattering feature appears at a different angle. Upon annealing in oxygen, the scattering feature practically vanishes, reflecting the loss of the structural integrity of the Ag-behenate film. We now turn our attention to APXPS data describing this annealing process from the point of view of chemistry.

Figure 4(a) shows C 1s XPS spectra for Ag-behenate/Si(001) corresponding to x-ray scattering patterns shown in Figs. 3(c) and 3(d) before and after annealing in oxygen. Because Ag-behenate contains a CH$_x$ backbone with 21 carbon atoms and a terminating carboxyl group (–COO), the XPS intensity in the C 1s region is expected to have its largest contribution from C–C species, generally appearing near 284 eV.[41] In addition, adventitious carbon species accumulate on surfaces exposed to air and contribute to the C 1s spectrum near 284 eV.[42] The bottom spectrum in Fig. 4(a) was taken in vacuum after introducing the sample into the chamber, with overlapping C–C and adventitious carbon peaks appearing in the C 1s region, along with a peak produced by the carboxyl group in Ag-behenate at 286.9 eV.[43,44] The ratio of these two peaks was ~10:1 [Fig. 4(a)]. This contrasts with the composition of the molecule, which has 22 C atoms, only one of which exists in a carboxyl group. Experimentally, the ratio of these two peaks not only reflects the ratio of each type of carbon species in the molecule but is also influenced by the presence of contaminant species on the sample, by the orientation of the molecules on the surface, and by the integrity of the molecular structure. Regarding the molecular integrity, Ag-behenate is known to decompose upon prolonged exposure to air and light, which can contribute to different spectral weights in the C 1s spectra, and create a diffuse photon scattering background. Hence, the vacuum XPS in the C 1s region in Fig. 4(a) reflects that Ag-behenate has undergone some decomposition, and the sample contains other carbon-containing species, potentially altering the area ratios of the relevant peaks. Figure 4(b) shows the Ag 3d spectra corresponding to each condition from Fig. 4(a). In vacuum, the Ag 3d spectrum contains a peak at 367.8 eV, characteristic of Ag$^+$.[45] The presence of a feature above 370 eV is indicative of Ag satellite features, which can contain contributions from Ag^0 and/or Ag partially oxidized by interaction in Ag-behenate.[46]

After characterizing the surface in vacuum, we added 1 Torr of O$_2$ gas into the chamber. Oxygen exposure reduced the intensity of the C–C peak at 284.5 eV, suggesting a reaction with some of the carbon species at the surface. At the same time, the intensity of the peak at 286.9 eV remained approximately the same as in vacuum. This indicates that the carboxyl groups in Ag-behenate do not rapidly decompose upon O$_2$ exposure in these conditions, even when parts of the molecule decompose slowly when exposed to light and ambient air conditions. The decrease in the C–C peak is accompanied by the appearance of a feature at 288.5 eV, characteristic of more highly oxidized carbon species resulting from exposure to O$_2$ gas.[47] In the C 1s region, when the sample was heated to 145 °C in 1 Torr of O$_2$, only a 10% decrease in the intensity of the C–C peak

was observed, indicating that the remaining carbon did not react readily with oxygen at this temperature. Nevertheless, the scattering feature generated by regularly spaced layers of Ag-behenate nearly vanished [Fig. 3(d)]. Ag-behenate undergoes thermally induced carbon chain folding above 120 °C, where it adopts a new molecular packing arrangement that decreases the Ag-behenate interlayer spacing.[39] This is consistent with our observation that the feature due to scattering from regularly spaced Ag-behenate layers nearly vanishes under these conditions.

The chemical transformation of Ag-behenate, as observed by APXPS, is consistent with the results of the simultaneous scattering experiments. Nevertheless, the altered packing arrangement of the Ag-behenate layers has a structure, which should also produce a scattering pattern detectable in the angular range of our GIXS system.[39] However, we note that the C–C and carboxyl intensities decreased somewhat while heating in oxygen, and at the same time, the BE of the Ag 3d peak shifted to 367.3 eV upon heating in O_2. This latter BE shift is characteristic of a transformation to Ag^{2+},[45] suggesting that the Ag atoms from the Ag-behenate layered structure further oxidize into AgO. The oxidation of Ag under these conditions could coincide with a change in the structure of the Ag-behenate layers, explaining the disappearance of the diffraction ring. Additionally, the diminished intensity of both the carboxyl and C–C peaks suggests that the molecules begin to decompose with some components becoming volatile.

V. CONCLUSIONS

These combined APXPS and APGIXS measurements on Ag-behenate illustrate the power of correlating chemical and structural transformations for samples in gas phase environments. Changes in the Ag-behenate layered structure were observed using APGIXS and were correlated with changes in the Ag oxidation state and carbon chemistry observed in the Ag 3d and C 1s XPS regions. Combining APXPS and APGIXS provided a simultaneous picture of the chemical state and structure of the sample and also provided a detailed picture of their evolution in an O_2 gas environment and different thermal conditions. Our approach to understanding correlations between structure and behavior is applicable in a variety of fields, where important phenomena often involve complex relationships between structure, chemistry, and activity.[5–15]

The geometry of APXPS measurements involves x rays incident on surfaces in a way that inherently enables scattering measurements in the reflection geometry (Fig. 1). Additionally, our development of a compact pivoting-UHV-manipulator to control the detector motion makes this configuration highly customizable. Using an x-ray transparent SiN_x membrane to isolate the x-ray detector enables GIXS measurements for samples in a wide variety of gas phase environments. These developments make it possible to retrofit many existing APXPS, XPS, and other experimental systems to include simultaneous (AP)-GIXS measurements with relatively low cost and effort.

Further related techniques can also be enabled using this approach. For example, X-ray photon correlation spectroscopy (XPCS) measures correlations in scattering intensities from a distribution of scattering centers illuminated by coherent photons. The evolution of the correlation between speckle patterns over time provides a measurement of the evolution of scattering center distributions in a sample.[48] This opens new possibilities to study dynamic systems and transformations on their natural timescales. Several soon-to-be-emerging diffraction limited synchrotron sources around the world will offer coherent flux intensities increased by orders of magnitude, allowing measurements with time resolution into the microsecond and nanosecond regimes.

AUTHORS' CONTRIBUTIONS

H.B. and S.N. initiated this project. H.K., S.R., A.K., and S.N. contributed to the system design. H.K. and S.N. performed the experiments with support from B.H.L. and M.B. Data analysis was performed by H.K. with support from Q.L., H.M., P.C., and F.B. H.K. and S.N. wrote this manuscript. S.N. supervised this project.

DATA AVAILABILITY

The data that support the findings of this study are available from the corresponding author upon reasonable request.

REFERENCES

[1]Y. Yuan and J. Huang, "Ion migration in organometal trihalide perovskite and its impact on photovoltaic efficiency and stability," Acc. Chem. Res. **49**(2), 286–293 (2016).

[2]B. Kiraly, A. N. Rudenko, W. M. J. van Weerdenburg, D. Wegner, M. I. Katsnelson, and A. A. Khajetoorians, "An orbitally derived single-atom magnetic memory," Nat. Commun. **9**, 3904 (2018).

[3]T. Shang, Y. Wen, D. Xiao, L. Gu, Y.-S. Hu, and H. Li, "Atomic-scale monitoring of electrode materials in lithium-ion batteries using *in situ* transmission electron microscopy," Adv. Energy Mater. **7**, 1700709 (2017).

[4]W. Gao, Z. D. Hood, and M. Chi, "Interfaces in heterogeneous catalysts: Advancing mechanistic understanding through atomic-scale measurements," Acc. Chem. Res. **50**, 787–795 (2017).

[5]M. F. Hochella, Jr., S. K. Lower, P. A. Maurice, R. L. Penn, N. Sahai, D. L. Sparks, and B. S. Twining, "Nanominerals, mineral nanoparticles, and Earth systems," Science **319**(5870), 1631–1635 (2008).

[6]A. S. Madden and M. F. Hochella, "A test of geochemical reactivity as a function of mineral size: Manganese oxidation promoted by hematite nanoparticles," Geochim. Cosmochim. Acta **69**(2), 389–398 (2005).

[7]M. F. Hochella, T. Kasama, A. Putnis, C. V. Putnis, and J. Moore, "Environmentally important, poorly crystalline Fe/Mn hydrous oxides: Ferrihydrite and possibly new vernadite-like mineral from the Clark Fork River superfund complex," Am. Mineral. **90**(4), 718–724 (2005).

[8]F. Tao, S. Dag, L.-W. Wang, Z. Liu, D. R. Butcher, H. Bluhm, M. Salmeron, and G. A. Somorjai, "Break-up of stepped platinum catalyst surfaces by high CO coverage," Science **327**, 850–853 (2010).

[9]S. R. Longwitz, J. Schnadt, E. K. Vestergaard, R. T. Vang, I. Stensgaard, H. Brune, and F. Besenbacher, "High-coverage structures of carbon monoxide adsorbed on Pt(111) studied by high-pressure scanning tunneling microscopy," J. Phys. Chem. B **108**, 14497–14502 (2004).

[10]B. Eren and M. Salmeron, "Predicting surface clustering at ambient conditions from thermodynamic data," J. Phys. Chem. C **123**, 8171–8176 (2019).

[11]B. Eren, D. Zherebetskyy, L. L. Patera, C. H. Wu, H. Bluhm, C. Africh, L.-W. Wang, G. A. Somorjai, and M. Salmeron, "Activation of Cu(111) surface by decomposition into nanoclusters driven by CO adsorption," Science **351**(6272), 475–478 (2016).

[12]B. Eren, D. Zherebetskyy, Y. Hao, L. L. Patera, L.-W. Wang, G. A. Somorjai, and M. Salmeron, "One-dimensional nanoclustering of the Cu(100) surface under CO gas in the mbar pressure range," Surf. Sci. **651**, 210–214 (2016).

[13]J. Kim, W. H. Park, W. H. Doh, S. W. Lee, M. C. Noh, J.-J. Gallet, F. Bournel, H. Kondoh, K. Mase, Y. Jung, B. S. Mun, and J. Y. Park, "Adsorbate-driven reactive interfacial Pt-NiO$_{1-x}$ nanostructure formation on the Pt$_3$Ni(111) alloy surface," Sci. Adv. **4**(7), eaat3151 (2018).

[14]F. Tao, M. E. Grass, Y. Zhang, D. R. Butcher, J. R. Renzas, Z. Liu, J. Y. Chung, B. S. Mun, M. Salmeron, and G. A. Somorjai, "Reaction-driven restructuring of Rh-Pd and Pt-Pd core-shell nanoparticles," Science **322**(5903), 932–934 (2008).

[15]Z. Tan, S. Chen, X. Peng, L. Zhang, and C. Gao, "Polyamide membranes with nanoscale turing structures for water purification," Science **360**(6388), 518–521 (2018).

[16]D. M. Meier, A. Urakawa, and A. Baiker, "Polarization-modulation infrared reflection-absorption spectroscopy affording time-resolved simultaneous detection of surface and liquid phase species at catalytic solid-liquid interfaces," Analyst **134**, 1779–1780 (2009).

[17]C. T. Herbschleb, P. C. van der Tuijn, S. B. Roobol, V. Navarro, J. W. Bakker, Q. Liu, D. Stoltz, M. E. Cañas-Ventura, G. Verdoes, M. A. van Spronsen, M. Bergman, L. Crama, I. Taminiau, A. Ofitserov, G. J. C. van Baarle, and J. W. M. Frenken, "The ReactorSTM: Atomically resolved scanning tunneling microscopy under high-pressure, high-temperature catalytic reaction conditions," Rev. Sci. Instrum. **85**, 083703 (2014).

[18]J. F. Creemer, S. Helveg, G. H. Hoveling, S. Ullmann, A. M. Molenbroek, P. M. Sarro, and H. W. Zandbergen, "Atomic-scale electron microscopy at ambient pressure," Ultramicroscopy **108**(9), 993–998 (2008).

[19]F. Tao, D. Tang, M. Salmeron, and G. A. Somorjai, "A new scanning tunneling microscope reactor used for high-pressure and high-temperature catalysis studies," Rev. Sci. Instrum. **79**, 0840101 (2008).

[20]S. B. Roobol, M. E. Cañas-Ventura, M. Bergman, M. A. van Spronsen, W. G. Onderwaater, P. C. van der Tuijn, R. Koehler, A. Ofitserov, G. J. C. van Baarle, and J. W. M. Frenken, "The ReactorAFM: Non-contact atomic force microscope operating under high-pressure and high-temperature catalytic conditions," Rev. Sci. Instrum. **86**, 033706 (2015).

[21]D. F. Ogletree, H. Bluhm, E. D. Hebenstreit, and M. Salmeron, "Photoelectron spectroscopy under ambient pressure and temperature conditions," Nucl. Instrum. Methods Phys. Res., Sect. A **601**, 151–160 (2009).

[22]A. R. Head, O. Karslıoğlu, T. Gerber, Y. Yu, L. Trotochaud, J. Raso, P. Kerger, and H. Bluhm, "CO adsorption on Pd(100) studied by multimodal ambient pressure X-ray photoelectron and infrared reflection absorption spectroscopies," Surf. Sci. **665**, 51–55 (2017).

[23]M. A. Marcus, A. A. MacDowell, R. Celestre, A. Manceau, T. Miller, H. A. Padmore, and R. E. Sublett, "Beamline 10.3.2 at ALS: A hard X-ray microprobe for environmental and materials sciences," J. Synchrotron Radiat. **11**, 239–247 (2004).

[24]G. Eres, C. M. Rouleau, Q. Lu, Z. Zhang, E. Benda, H. N. Lee, J. Z. Tischler, and D. D. Fong, "Experimental setup combining in situ hard X-ray photoelectron spectroscopy and real-time surface X-ray diffraction for characterizing atomic and electronic structure evolution during complex oxide heterostructure growth," Rev. Sci. Instrum. **90**, 093902 1–11 (2019).

[25]C. S. Fadley, "X-ray photoelectron spectroscopy: Progress and perspectives," J. Electron Spectrosc. Relat. Phenom. **178-179**, 2–32 (2010).

[26]D. E. Starr, Z. Liu, M. Hävecker, A. Knop-Gericke, and H. Bluhm, "Investigation of solid/vapor interfaces using ambient pressure X-ray photoelectron spectroscopy," Chem. Soc. Rev. **42**, 5833 (2013).

[27]D. F. Ogletree, H. Bluhm, G. Lebedev, C. S. Fadley, Z. Hussain, and M. Salmeron, "A differentially pumped electrostatic lens system for photoemission studies in the millibar range," Rev. Sci. Instrum. **73**(11), 3872–3877 (2002).

[28]P. Müller-Buschbaum, "A basic introduction to grazing incidence small-angle X-ray scattering," Lect. Notes Phys. **776**, 61–89 (2009).

[29]C. D. Liman, S. Choi, D. W. Breiby, J. E. Cochran, M. F. Toney, E. J. Kramer, and M. L. Chabinyc, "Two-dimensional GIWAXS reveals a transient crystal phase in solution-processed thermally converted tetrabenzoporphyrin," J. Phys. Chem. B **117**(46), 14557–14567 (2013).

[30]M. He, J. Li, M. L. Sorensen, F. Zhang, R. R. Hancock, H. H. Fong, V. A. Pozdin, D.-M. Smilgies, and G. G. Malliaras, "Alkylsubstituted thienothiophene semiconducting materials: Structure-property relationships," J. Am. Chem. Soc. **131**, 11930–11938 (2009).

[31]G. Kaune, M. A. Ruderer, E. Metwalli, W. Wang, S. Couet, K. Schlage, R. Röhlsberger, S. V. Roth, and P. Müller-Buschbaum, "In situ GISAXS study of gold film growth on conducting polymer films," ACS Appl. Mater. Interfaces **1**(2), 353–360 (2009).

[32]R. E. Winans, S. Vajda, B. Lee, S. J. Riley, S. Seifert, G. Y. Tikhonov, and N. A. Tomczyk, "Thermal stability of supported platinum clusters studied by in situ GISAXS," J. Phys. Chem. B **108**(47), 18105–18107 (2004).

[33]T. H. Metzger, I. Kegel, R. Paniago, A. Lorke, J. Peisl, J. Schulze, I. Eisele, P. Schittenhelm, and G. Abstreiter, "Shape, size, strain and correlations in quantum dot systems studied by grazing incidence X-ray scattering methods," Thin Solid Films **336**, 1–8 (1998).

[34]T. H. Metzger, I. Kegel, R. Paniago, and J. Peisl, "Grazing incidence x-ray scattering: An ideal tool to study the structure of quantum dots," J. Phys. D: Appl. Phys. **32**, A202–A207 (1999).

[35]A. Hexemer and P. Müller-Buschbaum, "Advanced grazing-incidence techniques for modern soft-matter materials analysis," IUCrJ **2**(1), 106–125 (2015).

[36]H. Bluhm, K. Andersson, T. Araki, K. Benzerara, G. E. Brown, J. J. Dynes, S. Ghosal, M. K. Gilles, H.-C. Hansen, J. C. Hemminger, A. P. Hitchcock, G. Ketteler, A. L. D. Kilcoyne, E. Kneedler, J. R. Lawrence, G. G. Leppard, J. Majzlam, B. S. Mun, S. C. B. Myneni, A. Nilsson, H. Ogasawara, D. F. Ogletree, K. Pecher, M. Salmeron, D. K. Shuh, B. Tonner, T. Tyliszczak, T. Warwick, and T. H. Yoon, "Soft X-ray microscopy and spectroscopy at the molecular environmental science beamline at the Advanced Light Source," J. Electron Spectrosc. **150**, 86–104 (2006).

[37]T. Hoshino, M. Kikuchi, D. Murakami, Y. Harada, K. Mitamura, K. Ito, Y. Tanaka, S. Sasaki, M. Takata, H. Jinnai, and A. Takahara, "X-ray photon correlation spectroscopy using a fast pixel array detector with a grid mask resolution enhancer," J. Synchrotron Radiat. **19**, 988–993 (2012).

[38]T. N. Blanton, T. C. Huang, H. Toraya, C. R. Hubbard, S. B. Robie, D. Louër, H. E. Göbel, G. Will, R. Gilles, and T. Raftery, "JCPDS-International Centre for Diffraction Data round robin study of silver behenate. A possible low-angle X-ray diffraction calibration standard," Powder Diffr. **10**(2), 91–95 (1995).

[39]T. N. Blanton, S. Zdzieszynski, M. Nicholas, and S. Misture, "In situ high-temperature X-ray diffraction study of phase transformations in silver behenate," Powder Diffr. **20**(2), 94–96 (2005).

[40]M. Nyam-Osor, D. V. Soloviov, Y. S. Kovalev, A. Zhigunov, A. V. Rogachev, O. I. Ivankov, R. V. Erhan, and A. I. Kuklin, "Silver behenate and silver stearate powders for calibration of SAS instruments," J. Phys.: Conf. Ser. **351**, 012024 (2012).

[41]M. Morkel, V. V. Kaichev, G. Rupprechter, H.-J. Freund, I. P. Prosvirin, and V. I. Bukhtiyarov, "Methanol dehydrogenation and formation of carbonaceous overlayers on Pd(111) studied by high-pressure SFG and XPS spectroscopy," J. Phys. Chem. B **108**, 12955–12961 (2004).

[42] G. Greczynski and L. Hultman, "C 1s peak of adventitious carbon aligns to the vacuum level: Dire consequences for material's bonding assignment by photoelectron spectroscopy," ChemPhysChem **18**, 1507–1512 (2017).

[43] J. Hasselström, O. Karis, M. Weinelt, N. Wassdahl, A. Nilsson, M. Nyberg, L. G. M. Pettersson, M. G. Samant, and J. Stöhr, "The adsorption structure of glycine adsorbed on Cu(110); comparison with formate and acetate/Cu(110)," Surf. Sci. **407**, 221–236 (1998).

[44] H. Ju, X. Feng, Y. Ye, L. Zhang, H. Pan, C. T. Campbell, and J. Zhu, "Ca carboxylate formation at the calcium/poly(methyl methacrylate) interface," J. Phys. Chem. C **116**, 20465–20471 (2012).

[45] T. C. Kaspar, T. Droubay, S. A. Chambers, and P. S. Bagus, "Spectroscopic evidence for Ag(III) in highly oxidized silver films by X-ray photoelectron spectroscopy," J. Phys. Chem. C **114**, 21562–21571 (2010).

[46] A. Dolatkhah, P. Jani, and L. D. Wilson, "Redox-responsive polymer template as an advanced multifunctional catalyst support for silver nanoparticles," Langmuir **34**, 10560–10568 (2018).

[47] T. E. Felter, W. H. Weinberg, G. Y. Lastushkina, A. I. Boronin, P. A. Zhdan, G. K. Boreskov, and J. Hrbek, "Ag(111), an XPS and UPS study of the kinetics of carbon monoxide oxidation over," Surf. Sci. **118**, 369–386 (1982).

[48] O. G. Shpyrko, "X-ray photon correlation spectroscopy," J. Synchrotron Radiat. **21**, 1057–1064 (2014).